

# PDR MODEL MAPPING OF PHYSICAL CONDITIONS VIA *SPITZER*-IRS SPECTROSCOPY OF H<sub>2</sub>: THEORETICAL SUCCESS TOWARD NGC 2023-SOUTH

Y. SHEFFER<sup>1</sup>, M. G. WOLFIRE<sup>1</sup>, D. J. HOLLENBACH<sup>2</sup>, M. J. KAUFMAN<sup>3</sup>, AND M. CORDIER<sup>3</sup>

*Draft version October 21, 2011*

## ABSTRACT

We use the IRS on *Spitzer* to observe the southern part of the reflection nebula NGC 2023, including the Southern Ridge, which is a photodissociation region *par excellence* excited by HD 37903. Five pure-rotational H<sub>2</sub> emission lines are detected and mapped over and around the Southern Ridge in order to compare with predicted level column densities from theoretical PDR models. We find very good agreement between PDR model predictions and emission line intensities and ratios measured with *Spitzer*, leading us to conclude that grain photoelectric heating sufficiently warms the gas to produce the observed H<sub>2</sub> line emission via collisional excitation. On the Southern Ridge, we infer a hydrogen nucleus density  $n_{\text{H}} \approx 2 \times 10^5 \text{ cm}^{-3}$  and radiation field strength  $\chi \approx 10^4$  relative to the local Galactic interstellar radiation field. This high value for  $\chi$  independently predicts a distance toward HD 37903 of 300 pc, and is consistent with the most recent *HIPPARCOS* results. Over the map we find that both  $n_{\text{H}}$  and  $\chi$  vary by a factor of  $\sim 3$ . Such 2-D variations provide clues about the underlying 3-D structure of the Southern Ridge field, which appears to be the tip of a molecular cloud. We also map variations in excitation temperature and the ortho-to-para ratio, the latter attaining values of  $\sim 1.5$ – $2.0$  on the Southern Ridge, and find that PDR modeling can readily reproduce observed ortho-to-para ratios that are  $< 3$  for rotational excitation dominated by collisional processes. Last, the stars Sellgren C and G are discovered to be resolved on archival *HST* images into two point sources each, with separations of  $\lesssim 0''.5$ .

*Subject headings:* infrared: ISM — ISM: clouds — ISM: individual objects (NGC 2023) — ISM: molecules — photon-dominated region (PDR) — Stars: individual (HD 37903)

## 1. INTRODUCTION

Photodissociation regions (PDRs) are regions in interstellar clouds in which far-ultraviolet ( $6 < h\nu < 13.6 \text{ eV}$ ; FUV) radiation plays a significant role in the heating and/or chemistry (Tielens & Hollenbach 1985). For example, PDRs are found in reflection nebulae and molecular cloud surfaces, where the radiation from nearby OB stars illuminates the clouds. The incident starlight is absorbed by dust and polycyclic aromatic hydrocarbons (PAHs) and is mostly used to excite the PAHs and heat the grains. However, a fraction ( $\sim 0.1$ – $1\%$ ) of the absorbed FUV starlight may be converted into energetic photoelectrons, which are ejected from PAHs and grains, and subsequently heat the gas. The strong FUV radiation acts as a beacon to illuminate the cloud structure, and to photodissociate, ionize, and excite gas phase chemical species, which otherwise would not be seen in emission. Thus, PDRs emit strong far-infrared continuum emission from grains, as well as infrared, submillimeter, and millimeter-wave line emission arising from the warm gas. The FUV radiation can affect the chemistry in molecular clouds to a depth of  $A_V \sim 5$  by maintaining the oxygen that is not tied up in CO in atomic form (Tielens & Hollenbach 1985; Hollenbach et al. 2009). This depth is comparable to the mean column density in giant molecular clouds

(Solomon et al. 1987; Heyer et al. 2009). The same PDR physics that is at work at the surfaces of molecular clouds also acts in the diffuse interstellar medium (Wolfire et al. 2003) and, therefore, much of the ISM is found in PDRs.

In general, the theoretical models (e.g., Sternberg & Dalgarno 1995; Wolfire et al. 2003; Kaufman et al. 2006; Le Petit et al. 2006) do a good job in predicting the atomic fine-structure line intensities and line ratios in PDRs; however, several observations of line emission from H<sub>2</sub> using *ISO* (Timmermann et al. 1996; Fuente et al. 1999; Draine & Bertoldi 2000) and *Spitzer* (Goldsmith et al. 2010) seem to indicate temperatures higher than those predicted by grain photoelectric heating alone. In addition, observations and modeling of high- $J$  lines of CO (Jaffe et al. 1990; Steiman-Cameron et al. 1997) would also indicate that models underestimate the gas temperature ( $T_{\text{gas}}$ ). Habart et al. (2011) found order-of-magnitude discrepancies between their PDR model results and *Spitzer* H<sub>2</sub> data for rotational levels  $J \geq 3$  toward mainly low-excitation PDRs. Dedes et al. (2010) were able to fit observations of high- $J$  CO lines by using spherical PDR models for an ensemble of clumps distributed in size and mass. Weingartner & Draine (1999) have suggested that radiation forces on grains increase the dust/gas ratio in PDRs thus leading to enhanced heating rates. Dissipation of turbulence (Falgaroni et al. 2005) and shocks (Habart et al. 2011) might also be an important source of heating in low-FUV field environments such as the Taurus molecular cloud (Goldsmith et al. 2010) or in the diffuse ISM.

Molecular hydrogen, H<sub>2</sub>, is a sensitive probe of PDRs

<sup>1</sup> Department of Astronomy, University of Maryland, College Park, MD 20742, USA; ysheffer@astro.umd.edu

<sup>2</sup> SETI Institute, 189 Bernardo Ave, Mountain View, CA 94043, USA

<sup>3</sup> Department of Physics and Astronomy, San Jose State University, One Washington Square, San Jose, CA 95192, USA

in our Galaxy (Allers et al. 2005) as well as in highly redshifted galaxies (Sheffer et al. 2009). The pure-rotational ( $v = 0$ ) transitions of  $H_2$  in the mid-IR are readily observed by space instruments, such as the IRS on *Spitzer* (Houck et al. 2004). The high spatial resolution ( $<10''$ ) of our *Spitzer* observations more clearly isolate the emission structures and different physical regions compared to the previous *ISO* observations. In general, transitions between low- $J$  levels of the  $v = 0$  state probe  $T_{\text{gas}}$  owing to their low critical densities, while the higher-excitation energy levels are pumped by FUV radiation and probe the radiation field strength and gas density (Sternberg & Dalgarno 1989; Burton et al. 1990).

This project has two main goals: first, to use  $H_2$  observations from *Spitzer*-IRS of the reflection nebula NGC 2023 to derive average gas physical conditions in the warm molecular regions and, second, to assess the reliability of PDR models to model the gas emission. In § 2 we track the changing values for the estimated distance of NGC 2023, present recent imaging results of the nebula, and describe our spectral mapping of the Southern Ridge (a.k.a. filament or bar, hereafter SR) area in NGC 2023 based on *Spitzer* data collected by the IRS. The intensities of pure-rotational emission lines from  $H_2$  are measured and converted into level column densities. These observables are compared in § 3 with model predictions based on updated Kaufman et al. (2006) models to show that a high level of agreement exists between theory and observation. Model parametrization allows us to map the 2-D distribution of total gas density and FUV strength, and to glimpse the 3-D structure of the nebula based on model fits. Section 3 also presents maps of the ortho- to para- $H_2$  (o- to p- $H_2$ ) ratio (OPR) and of excitation temperatures ( $T_{\text{ex}}$ ) for  $H_2$ , and concludes with a discussion of detected fine-structure line emission from Si II and Fe II. Section 4 is dedicated to the role of photoelectric heating compared to other processes. Finally, a concluding section provides a textual closure for the paper by emphasizing our main results.

## 2. THE TARGET AND THE DATA

### 2.1. What is the Distance to NGC 2023?

As a reflection nebula surrounding the hot B1.5 V star HD 37903, the issue of the distance of NGC 2023 is intimately tied to the distance of its central star, as well as being an essential ingredient in estimating the physical separation between HD 37903 and the SR. Most of the studies dealing with NGC 2023 over the last 30 years have employed a consistent range of values of 450–500 pc for the distance toward this object, as well as toward the entire nebular complex in Orion. However, assuming the depth is roughly the same as the projected extent, the angular size of the constellation of Orion predicts a depth to distance ratio of  $\sim 35\%$ , amounting to a range of  $\sim 140$  pc for a central value of 400 pc. Indeed, Anthony-Twarog (1982) derived a statistical distance toward Orion B stars of  $380^{+100}_{-80}$  pc. This shorter distance scale was employed by the Wyrowski et al. (1997) and Martini et al. (1999) studies of NGC 2023, but it was quickly abandoned in favor of the longer one based on the *HIPPARCOS* parallax of  $2.12 \pm 1.23$  mas (Perryman et al. 1997), placing HD 37903 at a rather imprecise distance of  $470^{+650}_{-170}$  pc.

However, very accurate parallax measurements with

very long baseline interferometry show the distance to the Orion Nebula to be 400 pc, with uncertainty of 2–6% (Sandstrom et al. 2007; Menten et al. 2007). Additional support for a shorter scale is provided by Caballero (2008), who derived a distance of  $334^{+25}_{-22}$  (or, less likely,  $385 \pm 15$ ) pc toward  $\sigma$  Ori, a star in the angular vicinity of HD 37903. Moreover, the cloud complex that includes NGC 2023 and the Horsehead Nebula appears to be in front of  $\sigma$  Ori (Mookerjee et al. 2009). We shall adopt  $350 \pm 50$  pc as the probable distance toward HD 37903 as suggested by Mookerjee et al. (2009). Clearly, HD 37903 is located at the very near side of the Orion nebular complex<sup>4</sup>, implying that the SR is separated from the star by a projected distance of  $(4.0 \pm 0.6) \times 10^{17}$  cm, or  $0.13 \pm 0.02$  pc.

### 2.2. Non-*Spitzer* Images

In order to become familiar with the appearance and structure of NGC 2023, we include here two high-quality public data products that have been obtained in recent years. The first is a near-IR image obtained at ESO (left panel of Figure 1), which clearly shows the structure of the nebula that heretofore had been hidden from visual view. The star HD 37903 has carved a quasi-spherical cavity into the dense molecular material out of which it formed. Consequently, its energetic FUV radiation illuminates the ridges of high-density gas, producing a reflection nebula and emission ridges that are detected in  $H_2$  line and dust (as well as PAH) continuum emission. Sellgren D, the eye-catching orange object below the pink SR, is resolved into at least three sources, whereas it was seen as an elongated object in previous renditions.

A portion of an archival image from the *Hubble Space Telescope* is also shown in Figure 1. Taken in red visible light with the ACS, it is the highest-resolution image ever taken of NGC 2023. The SR is resolved into an ensemble of clumps, all part of massive ridges of cloud tops that are basking in the FUV starshine of HD 37903. The SR was already known from ground-based work to be  $\sim 2''$  wide (Field et al. 1994, 1998), but the newly resolved clumps are smaller than that by a factor of a few. They are, on the other hand, much larger than the  $0''.05$  angular size of each pixel in the ACS field of view.

As a bonus, the (full) *HST* image also resolves two stars into their constituent components for the first time. These are Sellgren C near the western end of the SR, and Sellgren G, which is labeled on the ESO image. However, we cannot be certain that two actual binaries are involved, since young stellar objects, such as these PMS stars (Sellgren 1983), may be surrounded by a residual edge-on debris disks from the formation process, which might mimic a binary source. According to DePoy et al. (1990), their star 9 (Sellgren G) is consistent at the  $1-\sigma$  level with standard reddening vectors, i.e., it is not a convincing case of special extinction by a PMS “cocoon”. In both cases the components are  $0''.4 \pm 0''.1$  apart, or projected separations of  $\sim 150$  AU.

### 2.3. *Spitzer* Spectroscopy

We acquired *Spitzer*-IRS spectra of  $H_2$  emission lines toward NGC 2023 by employing the three modules SL,

<sup>4</sup> The short distance scale has now been confirmed by *HIPPARCOS*, see end of § 5 for details.

SH, and LH, as listed in Table 1, where the second letter ‘L’ or ‘H’ stands for low- or high-spectral resolution, respectively. The lower-resolution SL module is split into orders SL1 and SL2 and provides potential coverage of  $H_2$  emission lines from  $J = 4$ –9 levels, i.e., of transitions S(2) through S(7). However, owing to substantial blending with strong PAH features, we could detect only S(5) at  $6.91\ \mu\text{m}$  in SL2 data, and S(3) and S(2) at  $9.66$  and  $12.28\ \mu\text{m}$ , respectively, in SL1 spectra. SH also covers S(2), but at resolution  $\approx 10$  times higher than that of SL, and has exclusive coverage of S(1) from  $J = 3$  at  $17.03\ \mu\text{m}$ , whereas LH provides the only coverage of S(0) from  $J = 2$  at  $28.22\ \mu\text{m}$ .

The data were processed into cubes using the matching *Spitzer* Science Center pipeline version (S18.7.0) and CUBISM (Smith et al. 2007) version 1.7. All non-LH exposures were spatially degraded by re-gridding onto the (larger) pixels of the LH field of view prior to further analysis. Figure 2 shows the proper celestial location and orientation of the LH field over an  $8\ \mu\text{m}$  image from *Spitzer*-IRAC. With  $15 \times 14$  pixels in the LH field, each  $4''.46$  across, the irregular border of the combined intersection area of all modules measures  $\approx 1' \times 1'$  along the instrumental X and Y directions.

Emission line maps were constructed by using IDL/GAUSSFIT to fit line profiles and to derive integrated line intensities that included continuum fitting and removal. Table 2 lists derived GAUSSFIT parameters and their uncertainties for the case of map medians (dominated by off-SR pixels) and for the case of the single on-SR pixel LH[7:8], which coincides with the location of peak  $H_2$  emission. Figure 3 shows the spatial distribution of  $H_2$  emission for the five detected transitions S(0), S(1), S(2), S(3), and S(5). In these maps, the SR is a very prominent source of  $H_2$  line emission, with a partial coverage of additional emission from the South-Southeastern Ridge toward the instrumental top right corner. (Note that here, and in following Figures, the instrumental orientation of the LH map is to be employed in order to avoid both additional interpolation of the data and the wasteful white margins inherent in celestial orientation.) The  $H_2$  shows good agreement in position and orientation with the SR seen in the IRAC  $8\ \mu\text{m}$  image, which traces mainly PAH emission (Figure 2).

The target area observed by *Spitzer* toward NGC 2023 shows prominent and broad emission features from PAH molecules together with strong and narrow (unresolved) emission lines from  $H_2$ , see Figure 4. This spectrum was obtained by averaging 15 LH pixels that sample the emission from the SR in all four IRS modules. Two minor contributions from atomic species on the SR belong to [Fe II] and [Si II], at  $25.99$  and  $34.82\ \mu\text{m}$ , respectively, which are expected to be PDR observables (Tielens & Hollenbach 1985; Kaufman et al. 2006) and are presented in § 3.4. Two other fine-structure transitions commonly found in H II spectra, [Ne II] at  $12.81\ \mu\text{m}$  and [S III] at  $18.71\ \mu\text{m}$ , are detected at extremely weak levels of emission all over the map. We shall concentrate in this analysis on the  $H_2$  lines, comparing them with model predictions. The analysis of the PAH features shall be presented in a later paper (Peeters, et al. 2011, in preparation).

#### 2.4. IRS Calibration Issues

##### 2.4.1. Differential Extinction

We applied extinction corrections to our data consistent with previous studies of  $H_2$  line emission from NGC 2023. Burton (1993) found that  $A_K = 0.3$  mag from their vibrationally excited emission lines of  $H_2$ , yielding  $A_V = 2.8$ – $2.3$  mag for the range  $R_V = 3.1$ – $5.5$  (Mathis 1990), whereas Burton et al. (1998) mentioned that  $A_V$  is likely to be  $\sim 3$ – $5$  mag, or  $A_K \sim 0.3$ – $0.65$  mag. Draine & Bertoldi (1996) and Draine & Bertoldi (2000) adopted  $A_K$  of 0.2 and 0.5 mag, respectively. For our corrections we adopted  $A_K = 0.5$  mag, which corresponds to  $A_V = 3.8$ – $4.7$  mag.

Using the extinction curve of Mathis (1990), the extinction correction varies between 6–29%, with the largest correction applying to S(3). The latter value is similar in magnitude to systematic effects in the absolute calibration of *Spitzer*-IRS fluxes, estimated to be  $\sim 20$ – $25\%$  (Galliano et al. 2008; Dale et al. 2009). For the rotational levels  $J = 2$  and 5 with the lowest and highest extinction corrections, respectively, we determined that varying both  $N_J$  values by  $\pm 20\%$  shifts their derived  $T_{52}$  value (i.e.,  $T_{\text{ex}}$  of level  $J = 5$  relative to level  $J = 2$ ) by  $+3$  and  $-8\%$ . This smaller change, owing to a weak dependence on the ratio of column densities (since  $T_{52} \propto \ln[N_2/N_5]$ ), is consistent with Dale et al. (2009), who reported  $\pm 10\%$  for derived line ratios extracted from *Spitzer*-IRS data.

##### 2.4.2. Background Subtraction

Background contribution from zodiacal emission is always present toward celestial targets, as a function of space (direction) and time (date). Toward NGC 2023, dedicated background exposures were taken only for the SL observations, revealing a wavelength-averaged ratio of background to data of 10%. We employed the zodiacal emission calculator from SPOT, for each date and pointing center of each observation in order to compute the expected level of background emission for our data, and found good agreement between observed and calculated zodiacal emission for the SL data. Thus we are assured that subtraction of calculated zodiacal emission from data that lack background exposures does not lead to any significant errors. Furthermore, since our analysis concerns emission intensity following continuum subtraction, such intensities are insensitive to the presence of continuum-like background levels.

##### 2.4.3. Intensity Inter-Calibration

There is a significant wavelength overlap at  $9.97$ – $14.74\ \mu\text{m}$  between the SH and SL1 modules. Previous works have shown a continuum mismatch between modules, with different modules requiring different scale factors to bring the continuum into agreement. For example, Brandl et al. (2004), had to shift their SH data by  $+36\%$  and their SL1 data by  $+17\%$  relative to LL data, showing that in their case, the SL1 scale was higher by  $+16\%$  than the scale of the SH module. Quanz et al. (2007), on the other hand, found higher readings from SH data relative to SL1 data, and attributed these 8–25% scale shifts to different slit orientations relative to source emission. Beirão et al. (2008) found up to 50% differences in fits of PAH features based on SH and SL1 spectra.

We performed a pixel-wise  $\chi^2$  analysis of SH data versus SL1 data, which included background subtraction as well as SH resolution degradation to the lower spectral resolution of SL1 data. The absolute intensity scale of the SH data was found to be higher by 19% than that of SL1 data. Since we consider the higher signal-to-noise SL1 data to be more reliable spectrophotometrically, the SH (and LH) data were re-scaled by 0.84 prior to measuring integrated intensity values for the S(0), S(1), and S(2) lines.

The combined uncertainty in our measurements owing to the dominant calibration issues of absolute flux uncertainty and inter-module uncertainty is  $\lesssim 30\%$ .

### 2.5. Comparison of Spitzer IRS with ISO SWS

The extinction-corrected  $H_2$  line intensities were converted into level column densities using  $N_J = 4\pi I_J / A_J \Delta E_J \text{ cm}^{-2}$ , where  $N_J$ ,  $I_J$ ,  $A_J$ , and  $\Delta E_J$  stand for the column density, emission intensity, Einstein A-coefficient, and transition energy for each upper level  $J$ . The  $H_2$  rotational emission lines are quadrupole transitions and thus an optically thin conversion is appropriate for all environments in the ISM. For mapping purposes, this procedure was followed for each pixel over the field of view. To compare with previous ISO observations, we employ the mean on-SR  $H_2$  column density based on  $I_J$  values from 15 pixels that sample SR emission. These pixels were also employed in the extraction of the average on-SR spectrum shown in Figure 4. The SR-averaged  $\log N_J$  values for  $J = 2, 3, 4, 5$ , and  $7$  are 20.29, 19.77, 18.95, 18.60, and 17.48  $\text{cm}^{-2}$ , respectively.

ISO-SWS observations of pure rotational transitions toward the SR of NGC 2023 were shown in Figure 5 of Draine & Bertoldi (2000), from which we extracted  $N_J$  values for the five emission lines detected in our *Spitzer* data. These values were then rescaled by 1/1.8 in order to remove the arbitrary beam filling factor employed by Draine & Bertoldi (2000), resulting in  $\log N_J$  values of 20.44, 19.84, 18.90, 18.56, and 17.24  $\text{cm}^{-2}$ . Consequently we find *ISO* to *Spitzer* column density ratios of 1.4, 1.2, 0.9, 0.9, and 0.6, averaging  $1.0 \pm 0.3$ , which has the uncertainty expected for two data sets with  $\sim 20\%$  uncertainty each. Still, it is fascinating that the ratio appears to have a monotonic decline with increasing  $J$ , possibly related to differences in beam sizes employed for differing wavelength regimes on both spacecraft.

Habart et al. (2004) quote the (extinction-uncorrected) *ISO* observable  $I = 1.65 \times 10^{-5} \text{ erg s}^{-1} \text{ cm}^{-2} \text{ sr}^{-1}$  for the S(3) line, taken with a  $19''$  beam centered on a point  $60''$  due south of HD 37903. This position lies north of the SR and prevents us from directly comparing it with SR intensity values, however it still lies within our mapped region. We simulated this beam on our IRS map and found that the *Spitzer*  $H_2$  emission is 42% higher than the value given by Habart et al. (2004), hence a column density ratio of *ISO/Spitzer* = 0.7, which is consistent with the ratios given above. The agreement between IRS and SWS results is quite good considering the uncertainty in the *ISO* beam filling factors and extended source calibrations for both *ISO* and *Spitzer*.

## 3. MODELING SPITZER DATA WITH PDR MODELS

### 3.1. Model Parameters

In order to test the results of PDR models, we compare  $N_J(H_2)$  values derived from our observed emission lines toward NGC 2023 with values predicted by our PDR model (Kaufman et al. 1999, 2006). This model includes the calculation of  $H_2$  processes from the Le Petit et al. (2006) code as discussed in Kaufman et al. (2006). These include radiative excitation and dissociation, dissociation heating, collisional excitation and deexcitation, radiative cooling, and heating by deexcitation of excited levels. The o- $H_2$  to p- $H_2$  conversion on grains is included in the Le Petit et al. (2006) code as described in Le Bourlot (2000). We also include a factor of 2 enhanced  $H_2$  formation rate as suggested by Habart et al. (2004) and discussed in Kaufman et al. (2006). The OH and CO chemistry has been updated as in Wolfire et al. (2010) and we test models for normally-incident photons. The model output consists of the  $H_2$  column densities in each  $J$  level integrated along the normal to the PDR surface, as well as the normally emitted  $H_2$  line intensities. The rovibrational quadrupole transitions are all optically thin. We will vary two main model parameters to obtain a best fit to the observations while holding all others constant. These are the hydrogen nucleus density,  $n_H$ , and the incident radiation field,  $\chi$ , in units of the Draine (1978) interstellar radiation field. We use the notation that  $\chi$  is the ratio of FUV field incident on the surface of the PDR divided by the free-space field in the local interstellar radiation field. Thus  $\chi = F_{FUV} / 4\pi I_D$ , where  $F_{FUV}$  is the incident FUV flux and  $I_D = 2.2 \times 10^{-4} \text{ erg s}^{-1} \text{ cm}^{-2} \text{ sr}^{-1}$  is the Draine intensity for the local ISM.

In order to establish initial parameter values for  $n_H$  and  $\chi$ , as well limit their variation during modeling to values that are consistent with known ranges of other observables, we need independent methods for estimating  $n_H$  and  $\chi$ . Wyrowski et al. (2000) applied PDR model results to their observed angular separations between emission from  $H_2$  and C91 $\alpha$  toward NGC 2023. They found a range of  $n_H = 0.6\text{--}1.4 \times 10^5 \text{ cm}^{-3}$ , which agrees with previous findings that this is a relatively high-density PDR and provides us with an initial density value of  $n_H \approx 10^5 \text{ cm}^{-3}$ . The FUV field reaching the PDR gas from HD 37903 depends on the latter's luminosity and the projected (lower limit) physical separation between the two, which depends on the distance of NGC 2023 from Earth. For a B1.5 V star of  $12 M_\odot$  (Conti et al. 2008) we find an FUV luminosity of  $1.13 \times 10^4 L_\odot$ , based on Parravano et al. (2003). An angular separation of  $78''$  between the star and the SR results in an FUV field strength of  $\chi = 9.27 \times 10^8 / D^2$ , where  $D$  is the distance in pc to HD 37903. Using the adopted value of  $D = 350 \pm 50 \text{ pc}$  (§ 2.1) predicts a range of fairly high values for  $\chi$  of  $7.6_{-1.8}^{+2.7} \times 10^3$ . We shall explore a range of  $\chi$  values corresponding to  $\sim 2\text{-}\sigma$  variation around this central value.

In comparing normal model line intensities to observations there are several factors to keep in mind, which can be divided into two classes. One class includes factors that may increase the ratio of observed intensity to model intensity. The first factor is the possible presence of multiple PDRs along the line of sight,  $f_P$ . A second factor is the inclination angle ( $\theta$ ) of a single PDR layer relative to the line of sight. Limb brightening is expected

to occur for any PDR inclination  $\theta > 0^\circ$ , causing the source line intensity to appear brighter than a face-on ( $\theta \equiv 0^\circ$ ) model PDR by the factor  $f_\theta = 1/\cos(\theta)$ . Both factors can be lumped together as a single raising factor,  $f_+ = f_P f_\theta \geq 1$ .

The other class to consider includes factors that may decrease the ratio of observed intensity to model intensity. First is the fraction of the beam area that is filled by the source emission,  $f_B$ . A second factor involves the incidence angle  $\phi$  of FUV illumination, which affects the penetration depth of the radiation field. The intrinsic (deprojected) geometry of the exciting star (HD 37903) to the SR should produce a range of values between strictly normal ( $\phi \equiv 0^\circ$ ) and strictly parallel ( $\phi \equiv 90^\circ$ ) incidence, depending on the details of the shapes of gas clumps on the SR. For any value of  $\phi > 0^\circ$ , the intensity of observed  $H_2$  emission is cut down by  $\cos(\phi)$  owing to the oblique path of the FUV photons through the gas layer, and thus we have for the lowering factor  $f_- = f_B f_\phi \leq 1$ .

The effects of the raising and lowering factors obviously work in opposite directions, such that the total effective ratio of data to model is  $f_{\text{eff}} = f_+ f_- = f_P f_\theta f_B f_\phi$ . Effective ratios for map pixels will be derived as logarithmic differences (or model "shifts") in § 3.2 via matching of absolute model  $N_J$  values between models and data. The value of  $f_{\text{eff}}$  only tells us whether  $f_+$  or  $1/f_-$  is the dominant effect, but not the actual values of any individual factors involved.

### 3.2. Absolute Column Densities as a Function of $J$

#### 3.2.1. A Single Normal Model

The absolute column density values,  $N_J(H_2)$ , constitute our primary means of comparing PDR model results with the observations. Figure 5 illustrates such a comparison for a single on-SR pixel, where a run of observed  $N_J$  values vs  $E_J$ , the level energy above the ground state, is compared with output from the best matching model. For illustration purposes, data are shown both before and after extinction correction is applied. The best match between models and data was determined from the smallest root mean square deviation (RMSD) of the differences in dex between modeled and observed absolute  $N_J$  values. In this way, both relative  $N_J$  ratios between even- and odd- $J$  levels, as well as global absolute  $N_J$  values, were being fitted with the best-matching model for each pixel. The RMSD-minimizing search for  $f_{\text{eff}}$  was performed via globally shifting the  $N_J$  values of each ( $n_H$ ,  $\chi$ ) model in steps of 0.01 dex relative to the data, over a range of  $\pm 1.0$  dex. (Larger ranges of up to  $\pm 10$  dex were tested, but did not improve the fits.) With a minimum RMSD value of 0.050 dex ( $\pm 12\%$ ) in Figure 5, it is obvious that very good agreements can be found between observed and modeled column densities in terms of the overall shape of the  $N_J$  curve.

As a test case, we fit several regions with fixed values of  $n_H = 10^5 \text{ cm}^{-3}$  and  $\chi = 5 \times 10^3$ . The median RMSD value on the SR is 0.144 dex, or a difference of 39% between data and models, i.e., clearly not fitting the data within the expected observational uncertainties. See Table 3 for a listing of results for fixed  $n_H$  and  $\chi$  that include other regions around the SR. Owing to the poor fit by a single model of fixed parameters, better agreement be-

tween data and models is expected from expanded ranges of the two parameters  $n_H$  and  $\chi$ .

#### 3.2.2. Expansion to a Multi-Model Grid

In order to reveal density and FUV flux variations, and thus take advantage of the mapping performed by the IRS, we have generated a grid of models over the  $n_H$  vs  $\chi$  parameter space. The grid of 49 normal models used here covers 0.6 dex in  $n_H$  and 0.6 dex in  $\chi$  with a step size of 0.1 dex. It is a subset of a larger grid comprising of 210 models, most of which did not fit any of the observed  $N_J$  curves. The parameter ranges of  $n_H = 0.5\text{--}2 \times 10^5 \text{ cm}^{-3}$  and  $\chi = 4\text{--}16 \times 10^3$  were found to provide much better fits (smaller RMSD) than using a single model over the entire map. The results of this multi-model fit are shown in Figure 6.

In this Figure we see that the highest density values of  $2 \times 10^5 \text{ cm}^{-3}$  are found on the SR, as well as on its neighbor, the SSE ridge. The range of  $n_H$  over the entire map is in very good agreement with that given by Wyrowski et al. (2000). The  $\chi$  map shows an enhancement of the FUV field on the SR of  $\chi = 10^4$ , which is  $\sim 30\%$  higher than  $7.6 \times 10^3$ , the central value expected according to the distance to NGC 2023 (§ 3.1), but is nonetheless consistent with the upper  $1\text{-}\sigma$  value for the expected  $\chi$ . (In fact, our initial comparison with expected  $\chi$  values based on the longer distance scale of 450–500 pc for NGC 2023 had resulted in model-to-expectation ratio of  $2.4^{+0.3}_{-0.2}$ . Such a very significant discrepancy prompted us to investigate the issue of the distance to HD 37903 more thoroughly, as reported in § 2.1). Taken at face value, a prediction of  $\chi = 10^4$  means that HD 37903 could be even closer by 1 sigma than the adopted short distance scale, i.e., 300, instead of 350, pc away<sup>5</sup>.

Both parameters diminish farther from the SR, except for regions with high  $\chi$  values farther to the North of the SR (lower right corner) that have smaller (projected) distance from the exciting star, HD 37903. The median RMSD value for the entire map area is 0.062 (Table 3). Note that for the SR this value has improved by a factor of  $>2$  relative to the single-model fit. The highest values of the global shift are also found on the SR, where the median is  $-0.13$  dex, or  $f_{\text{eff}} = 0.74$ . Most of the mapped (off-SR) area has a value of  $f_{\text{eff}} \sim 0.49$ , hence 1.5 times smaller than the on-SR value.

#### 3.2.3. Comparing $f_{\text{eff}}$ with Previous Results

The  $f_{\text{eff}}$ -corrected RMSD median of 0.062 shows that the combination of spatially higher-resolution data from *Spitzer*-IRS and recent improvements in PDR models appears to yield a very good level of agreement of 15% between observations and predictions of  $H_2$  emission. Over the map (Fig. 6) we find that  $-0.57 \leq \log f_{\text{eff}} \leq -0.09$ , or  $0.27 \leq f_+ f_- \leq 0.81$ , a variation by a factor of 3. Since  $f_+ f_- < 1$  for all pixels,  $f_-$  is the dominant factor for comparing models to observations of this region (i.e.,  $f_+ < 1/f_-$ ).

In their modeling of the SR, Draine & Bertoldi (1996) corrected the data from Hasegawa et al. (1987) by using

<sup>5</sup> This distance of 300 pc has now been confirmed by *HIPPARCOS*, see end of § 5 for details.

a beam filling factor of  $f_B = 1/6$ , and employed an inclination correction of  $f_\theta = 5$ , or  $\theta \approx 78^\circ$ . Their  $f_{\text{eff}} = f_\theta f_B = 0.83$  is closely matching the higher values found on our map. Draine & Bertoldi (2000) used the same  $f_\theta$  from Draine & Bertoldi (1996), but  $f_B = 1/1.8 = 0.56$ , resulting in  $f_{\text{eff}} = 2.8$ , a value  $>3$  times higher than our map's largest value of 0.81. Kaufman et al. (2006) used a proxy for the beam factor in the form of two-phased  $\text{H}_2$  medium (Steiman-Cameron et al. 1997), in which the dense gas from the SR was contributing at a level of 20%, and thus in effect using  $f_B = 0.2$ . In addition, they used  $f_\theta = 6$  in order to achieve a match between data and models. In short, this amounts to using  $f_{\text{eff}} = f_\theta f_B = 1.2$ , a value higher by  $\sim 50\%$  than our map's highest value. The contributions of multiple PDRs along the line of sight,  $f_P$ , and the angle of FUV illumination,  $f_\phi$ , were not explicitly mentioned by these studies.

We first consider the effects of varying  $f_B$  while holding the other factors fixed. Adopting the assumption of  $f_P f_\phi = 1$ , and using  $f_\theta = 5$  on the SR, as per Draine & Bertoldi (1996), we find  $f_B = f_{\text{eff}}/f_\theta = 0.74/5 = 0.148$ . However, off the SR, where values of  $f_{\text{eff}}$  are smaller, i.e.,  $f_{\text{eff}} = f_\theta f_B = 0.49$  (Table 3), the implied beam filling factor would also be smaller,  $f_B = 0.49/5 = 0.098$ . This trend is not likely since away from the SR, the source is more extended and not as concentrated as the SR, and therefore we expect  $f_B$  to become larger (approaching 1), not smaller. Thus we conclude that it is not  $f_B$  that is driving down the values of  $f_-$  (and thus of  $f_{\text{eff}}$ ) away from the SR. In the next section we explore the possible 3-D shape of the SR and show how a simultaneous reduction in both  $f_\phi$  and in  $f_\theta$  may explain the smaller off-SR values of  $f_{\text{eff}}$ .

### 3.2.4. Clues for 3-D Nebular Structure?

Our map exhibits  $f_{\text{eff}}$  below unity, with values decreasing away from the SR and possibly indicating a dominant reduction in any of the three factors  $f_P$ ,  $f_\theta$ , or  $f_\phi$ . All three factors are related to the 3-D structure of the nebula and their variability over the map should be helpful in deciphering the relative configuration between on-SR and off-SR regions.

Let us define  $\alpha$  as the angle at the source between our line of sight and the direction of incident FUV radiation from HD 37903. A contour plot of the product  $f_\theta f_\phi = \cos(\phi)/\cos(\theta)$  is shown in Figure 7, based on the relationship  $\alpha = \theta \pm \phi$ , or  $\phi = |\alpha - \theta|$ . The lower half of the figure includes the values  $f_\theta f_\phi < 1$ , although geometric configurations toward the lower right corner are excluded owing to the FUV source dipping below the horizon of the PDR face. There are two lines on the map where  $\phi = \theta$ , leading to  $f_\theta f_\phi = 1$ . One is where  $\phi = \theta = \alpha/2$ , as indicated by the diagonal line, and the other is where  $\alpha = 0^\circ$ , hence along the ordinate. Between these two lines and for any given  $\theta$ ,  $f_\theta f_\phi$  reaches a maximum when  $0^\circ \leq \alpha \leq 90^\circ$ , along the line  $\phi = 0^\circ$  where  $\cos(\phi) = 1$  and  $\theta = \alpha$ .

The impression from Figure 1 is that HD 37903 is located at the center of a bubble, and that the SR (as well as other ridges of intense emission) is marking the irradiated boundaries of the bubble. We may thus assume that  $\alpha$  is not too far from  $90^\circ$ , and thus the value of  $f_\theta f_\phi$  is expected to be near its maximal value. Furthermore,  $f_\theta$  probably achieves its highest value on the SR, assuming a

near edge-on view of the bubble's boundary. Away from emission ridges no such narrow features are seen, and thus moving away from the SR would result in lowering of the value of  $f_\theta f_\phi \rightarrow 1$ , as  $\phi \rightarrow \theta$ . For the spherical bubble scenario, we expect that  $45^\circ \lesssim \alpha \lesssim 135^\circ$ , which results in  $0.5 \lesssim f_\phi \leq 1.0$  and thus yielding  $f_\theta f_\phi > 1$  for any  $f_\theta > 2$ . This constraint is certainly true for  $\theta = 78^\circ$ , the nominally adopted value from Draine & Bertoldi (1996).

One way to achieve a 3-D configuration such that  $f_{\text{eff}}$  becomes smaller with distance from the SR is to assume that the molecular cloud banks have a quasi-pyramidal cross section. A cartoon that presents such a configuration is shown in Figure 8. [An earlier, albeit more simplified, cartoon was given in Figure 4 of Field et al. (1994).] Thus the southern slope of the SR may face our line of sight (with smaller  $\theta$  and  $f_\theta \rightarrow 1$ ), while the surface normal is at a larger  $\phi$  ( $f_\phi \rightarrow 0$ ) from the direction to HD 37903. In this case, starshine can still hit directly in a normal fashion the top of the SR that rise toward the star (as can be seen in Figure 1), but the off-SR gas is facing away from HD 37903 and is receiving slanted, and thus reduced, levels of FUV flux. In particular, still keeping a range of  $45^\circ \lesssim \alpha \lesssim 135^\circ$ , but assuming a  $45^\circ$  turn of the viewed slab toward our line of sight (e.g.,  $\theta = 78^\circ - 45^\circ = 33^\circ$ ) allows for a range of  $\phi \geq 12^\circ$  such that  $0.00 \leq f_\phi \leq 0.98$ . In other words, relative to on-SR values, the off-SR pyramidal slope provides a combination of smaller  $\theta$  and larger  $\phi$  that can readily achieve  $f_\theta f_\phi \ll 1$ , thus accounting for the observed reduction in  $f_{\text{eff}}$  away from the SR.

In this picture the SR is a manifestation of one ridge of clouds forming the outer layer of the much larger, denser, and darker molecular cloud. This cloud was outlined by  $\text{HCO}^+$  via the millimeter observations of Wyrowski et al. (2000), whose Figures 3 and 4 clearly show that the PDR ( $\text{H}_2$  and C recombination line emission) is located on the HD 37903-facing side of the denser structure. Indeed, the more opaque off-SR sight line may also explain any potential reduction in  $f_P$  relative to the on-SR sight line, thus providing a 3-D scenario that simultaneously reduces all three factors affecting  $f_{\text{eff}}$ .

## 3.3. Excitation Diagrams of $\text{H}_2$

### 3.3.1. Construction and Interpretation

While it has been understood since the earliest observations (Gatley & Kaifu 1987; Hasegawa et al. 1987) that ro-vibrational emission in NGC 2023 is dominated by FUV fluorescence, the situation regarding rotational emission from the  $v = 0$  state could depend on both collisional and radiative excitations. From our models we find that the S(0), S(1), and S(2) lines are produced at PDR depths where  $\text{H}_2$ - $\text{H}_2$  collisions thermalize level populations owing to collisional deexcitation rates that are much higher than radiative decays. For the lower  $T_{\text{gas}}$  involved ( $< 300$  K), relevant critical densities of the  $J = 2, 3$ , and 4 levels for  $\text{H}_2$ - $\text{H}_2$  collisions are 20, 360, and  $5100 \text{ cm}^{-3}$ , respectively, clearly below the inferred gas density of  $\sim 10^5 \text{ cm}^{-3}$ . The S(3) and S(5) lines arise at shallower depths near the PDR surface, where the gas is warmer and  $\text{H}_2$ -H collisions dominate the excitation. With respective critical densities for collisions with H (at  $\sim 600$  K) of  $3 \times 10^4$  and  $1.8 \times 10^5 \text{ cm}^{-3}$ , the upper levels  $J = 5$  and 7 are fully and marginally thermalized, re-

spectively, by such collisions. This establishes that the excitation temperatures of the  $\text{H}_2$  derived directly from observations are more closely associated with the gas kinetic temperature achieved through photoelectric heating than with the FUV pumping rate of the  $\text{H}_2$ .

In addition to (model-derived) gas density and FUV intensity, two other facets of  $\text{H}_2$  microphysics are the o- $\text{H}_2$  to p- $\text{H}_2$  ratio (Burton et al. 1992) and the excitation temperatures of rotational-level populations. Values of the OPR,  $T_{\text{ex}}$ , and ground-state population ( $N_0$ ) may be directly extracted from excitation diagrams employing  $\ln N_J/g_J$  vs  $E_J$ , as shown in Figure 9. For gas at LTE and with a single value of  $T_{\text{ex}}$ , the populations obey an exponential (Boltzmann) distribution so that the excitation function is a straight line having a slope of  $-1/T_{\text{ex}}$ . However, when the emitting region includes a range of  $\text{H}_2$  excitation temperatures the resulting function will be curved.

Each excitation curve may be approximated by a sum of two asymptotic straight lines representing two independent single- $T_{\text{ex}}$   $\text{H}_2$  components. One is a “cold” component with  $T_{\text{ex}}^{\text{cold}} \approx T_{32}$  and the other is “hot” with  $T_{\text{ex}}^{\text{hot}} \approx T_{75}$ . Extrapolation through  $E_1$  and  $E_0$  provides estimates of the ground state column densities  $N_1$  and  $N_0$ . However, this method of estimating the  $\text{H}_2$  column is sensitive to only those regions that are warm enough to emit in the rotational transitions and thus neglects the colder interior gas. In addition, owing to the monotonically declining character of the  $-1/T_{\text{ex}}$  curve, the straight line fits tend to overestimate  $T_{\text{gas}}$  (via  $T_{10}$ ) in the emitting regions.

In the case of  $\text{H}_2$ , the statistical weights  $g_J$  include a  $2J+1$  factor from orbital statistics and the nuclear factor of 3 for odd- $J$  levels. An excitation curve with a misalignment (zigzag) between odd- and even- $J$  populations is the indication that the  $\text{OPR} \neq 3$ . The average OPR between observed columns in odd- and even- $J$  states may be determined by de-zigzagging the curve. A fitting procedure was accomplished by shifting the odd- $J$   $N$  values toward the even- $J$  levels, with the resulting de-zigzagged curve of smallest RMSD providing the observed value of the OPR.

### 3.3.2. Mapping the OPR

Under local thermal equilibrium (LTE) and  $T \geq 300$  K, o- $\text{H}_2$  is three times more abundant than p- $\text{H}_2$ , hence  $\text{OPR} \equiv 3$ , owing to nuclear statistics. The OPR, which is initially set at the time  $\text{H}_2$  is formed on a surface of a dust grain, can be changed over time via collisions between  $\text{H}_2$  molecules and other gas constituents including H and  $\text{H}^+$ , and through accretion and subsequent ejection from grains (Burton et al. 1992; Sternberg & Neufeld 1999; Le Bourlot 2000). Radiative processes in  $\text{H}_2$  cannot change an original OPR value since they involve quadrupole transitions of  $\Delta J = 0, \pm 2$  in the ground electronic state. The first evidence for  $\text{H}_2$  molecules with  $\text{OPR} \neq 3$  in the ISM was provided by Hasegawa et al. (1987), who observed vibrationally excited  $\text{H}_2$  with  $\text{OPR} = 1.4\text{--}2.0$  toward the SR of NGC 2023. Sternberg & Neufeld (1999) calculated that an OPR value of 1.7 would be observed in vibrationally excited  $\text{H}_2$  even from a gas with o- $\text{H}_2$ /p- $\text{H}_2 = 3$ , owing to differences in pumping rates caused by the propensity of o- $\text{H}_2$  to self shield before p- $\text{H}_2$ . Thus, definitive evidence

of OPR other than 3 in a PDR has remained elusive. Recent measurements of the OPR in shocked gas, using pure rotational transitions of  $\text{H}_2$ , show more definitively that the ratio can differ from 3 owing to time dependent effects of the OPR conversion (e.g., Neufeld et al. 2006; Maret et al. 2009; Neufeld et al. 2009).

A de-zigzagging procedure was repeated for all data pixels in the field of view, yielding the OPR map in Figure 10. First, the global range of OPR variation over the map is  $0.9\text{--}2.0$ , or  $\approx 1.5\text{--}2.0$  inside the 75% intensity contour on the SR. This departure from  $\text{OPR} = 3$  is very similar to previous results (Hasegawa et al. 1987; Burton 1993; Fleming et al. 2010). Second, the highest OPR values are not aligned with SR intensity contours, but are found to be shifted toward the north, in the direction of the exciting star, HD 37903. This phenomenon is corroborated by OPR values on the star-facing side of the neighboring South-Southeastern Ridge.

Modeled OPR values are determined by a variety of conversion processes between o- and p- $\text{H}_2$ , with the dominant ones shown in Figure 11. Local OPR values are  $\gtrsim 3$  throughout shallow PDR layers with  $A_V \lesssim 1$ , but rapidly decline to  $\ll 1$  for  $A_V \gtrsim 2$ . We performed an identical de-zigzagging analysis of  $N_J$  values from the PDR model output. The integrated OPR value was found to be 1.8, in agreement with observations. In other words, the PDR model, with its various routes of o- $\text{H}_2 \rightleftharpoons$  p- $\text{H}_2$ , provides a close match to the run of  $T_{\text{ex}}$  and  $\text{H}_2$  level abundances that closely duplicates the observed OPR in the  $J = 2\text{--}7$  states. This result is important in showing that a steady-state PDR model can naturally (i.e., without adjustments) reproduce observed OPR values that are  $\neq 3$ , based on integrated columns through the entire PDR, without recourse to explanations involving time dependent effects. We emphasize that owing to collisional domination, the  $\text{H}_2$  rotational populations studied here should not be affected by differential self shielding effects (Sternberg & Neufeld 1999).

### 3.3.3. Mapping $T_{\text{ex}}$ and $N_0$

Values of  $T_{\text{ex}}$  derived from our *Spitzer* data are shown in the upper panels of Figure 12. Comparing the OPR map of Figure 10 with the  $T_{\text{ex}}^{\text{cold}}$  map, we see that the highest  $T_{\text{ex}}^{\text{cold}}$  values are found on the side of the SR facing away from HD 37903, where OPR values are lower, and vice versa.

Overall, the observed range of OPR values is lower than their LTE values for the observed range of  $T_{\text{ex}}^{\text{cold}}$ . Specifically, a range of  $\text{OPR} = 0.9\text{--}2.0$  may be obtained under LTE from a temperature range of  $74\text{--}118$  K. All observed  $T_{\text{ex}}$  values derived from these data, as well as the  $T_{\text{gas}}$  model values (§ 4), are  $>144$  K and thus would predict an LTE OPR of  $\geq 2.4$  over the entire map. In other words, the  $\text{H}_2$  has a lower OPR than values corresponding to all indicators of  $T_{\text{gas}}$ . (However, as previously remarked, extrapolations of  $T_{32}$  to lower- $J$  levels tend to overestimate  $T_{10}$ , which is not observed via rotational lines.) Although this result is derived strictly from observed  $N_J$  values, we may use the model to explain this effect thanks to the very good reproduction of  $N_J$ ,  $T_{\text{ex}}$ , and the OPR by our PDR model. We suggest that when  $T_{\text{ex}}$  and the OPR are calculated from the integrated columns,  $T_{\text{ex}}$  is weighted toward  $T_{\text{gas}}$  in the line emitting regions, while the OPR is being decoupled

from  $T_{\text{gas}}$  owing to increasing influence of  $T_{\text{dust}}$ . Indeed, beyond  $A_V \approx 1.5$  the OPR is dominated by the  $\text{o-H}_2 \rightarrow \text{p-H}_2$  conversion process via  $\text{H}_2$  accretion onto cold dust grains (Figure 11). These grains have  $T_{\text{dust}} \ll T_{\text{gas}}$ , thus inducing lower integrated OPR values than LTE predictions based on  $T_{\text{gas}}$ .

The two lower panels of Figure 12 present the derived  $N_0$  populations of “cold” and “hot”  $\text{H}_2$ , as defined by the two upper  $T_{\text{ex}}$  panels. It is seen that colder  $\text{H}_2$  is uniformly spread over the map, but that the hotter  $\text{H}_2$  population is found concentrated on the bright ridges of highest intensity. This picture of correlation between regions of higher  $\chi$  values and hotter  $\text{H}_2$  is confirmed by the distribution of  $T_{\text{ex}}^{\text{hot}}$  in the same Figure. Thus observables and derived characteristics that show the distribution of hotter, excited  $\text{H}_2$  levels, also track regions with higher FUV radiation fields.

From a given value of  $N_0$  and a single- $T_{\text{ex}}$  level population distribution, the total  $\text{H}_2$  column density can be estimated. Using the partition function formula from Herbst et al. (1996) gives  $N_{\text{tot}}^{\text{cold}} \approx 0.0247 N_0^{\text{cold}} T_{\text{ex}}^{\text{cold}} = 2.4 \times 10^{21} \text{ cm}^{-2}$ . We may then employ  $N_{\text{tot}}$  to estimate  $n(\text{H}_2)$  for an assumed depth along the line of sight. At the adopted distance of NGC 2023, the SR angular width of  $\sim 2''$  corresponds to  $\sim 10^{16} \text{ cm}$ , which closely approximates the model depth of the warm emitting region. Employing  $f_\theta \approx 5$  we have  $n(\text{H}_2) \approx N_{\text{tot}}^{\text{cold}} / 5 \times 10^{16} \approx 5 \times 10^4 \text{ cm}^{-3}$ . The corresponding  $n_{\text{H}} = 2 \times n(\text{H}_2)$  is, of course, higher. This estimate, which is PDR model independent, provides a strong support for the case that the SR is a relatively high-density region, and that our PDR modeling computes very reasonable values for the two parameters  $n_{\text{H}}$  and  $\chi$ . Note that, just like  $N_0^{\text{cold}}$ , the observational estimates of both  $N_{\text{tot}}^{\text{cold}}$  and  $n(\text{H}_2)$  are lower limits owing to the underestimation of the unobserved (but higher-valued)  $J = 0$  and 1 level populations.

#### 3.4. Atomic Line Emission from Si and Fe

In § 2.3 we remarked that the only two PDR-generated atomic emission lines present in our NGC 2023 spectra belong to [Si II] and [Fe II]. The former line at  $34.82 \mu\text{m}$  is detected from the SR by *Spitzer* with an average intensity of  $2.1 \times 10^{-5} \text{ erg s}^{-1} \text{ cm}^{-2} \text{ sr}^{-1}$ . This is twice the observed intensity estimated by Kaufman et al. (2006) based on the *ISO* data.

The Kaufman et al. (2006) model prediction for [Si II] intensity was  $6 \times 10^{-5} \text{ erg s}^{-1} \text{ cm}^{-2} \text{ sr}^{-1}$  based on  $n_{\text{H}}$  and  $\chi$  from *ISO*  $\text{H}_2$  observations. Their model used a gas phase silicon abundance of  $\text{Si}/\text{H} \sim 1.7 \times 10^{-6}$  for a depletion of  $\sim 20$  relative to the solar abundance. The difference between model and observed intensity was attributed to additional depletion by a factor of  $\sim 6$  compared to the model value. There is a strong dependence of model line intensities on both  $n_{\text{H}}$  and  $\chi$  so that our PDR parameter values, which are based on the *Spitzer*  $\text{H}_2$  observations (§ 3.2.2) lead to even higher predicted intensity values. Figures 1 and 2 of Kaufman et al. (2006) present  $(n_{\text{H}}, \chi)$  grids for normal models, predicting [Si II] and [Fe II] emission intensities, respectively. We use those grids and depletions for comparison with observed values, and do not repeat such calculations here since, as far as atomic emission computations are concerned, essentially the same models used by Kaufman et al. (2006)

are used here.

Our  $\text{H}_2$  mapping of the SR indicated a  $\log(n_{\text{H}}, \chi)$  solution of (5.2, 4.0), for which the predicted [Si II] intensity is  $\sim 10^{-3} \text{ erg s}^{-1} \text{ cm}^{-2} \text{ sr}^{-1}$ . Next, this value needs to be corrected for beam filling. As a rough estimate we use the ratio of the diffraction limit at  $35 \mu\text{m}$  ( $8''.5$ , Houck et al. 2004) over the SR limit of  $2''$  to get  $\sim 2 \times 10^{-4} \text{ erg s}^{-1} \text{ cm}^{-2} \text{ sr}^{-1}$ . Consequently, [Si II] predictions based on our PDR model maps are  $\sim 10$  times higher than the observed value. To bring our observations and model into agreement, the gas-phase Si/H abundance would have to be  $\sim 1.7 \times 10^{-7}$ , i.e., depleted by a factor of  $\sim 200$  relative to the solar Si abundance. Our results are consistent with previous investigations (Draine & Bertoldi 2000; Kaufman et al. 2006) in finding that a large depletion of gas-phase Si is required to bring models and observations into agreement.

As for the weaker [Fe II] line at  $25.99 \mu\text{m}$ , it has 25% of the emission intensity of [Si II], or  $5 \times 10^{-6} \text{ erg s}^{-1} \text{ cm}^{-2} \text{ sr}^{-1}$ . This is the first reported detection of [Fe II] emission in NGC 2023. The model-predicted [Fe II] to [Si II] intensity ratio is  $\sim 0.1$ , indicating that the Fe/Si abundance ratio is  $\sim 2.5$  times higher than the values adopted in the models. Since the Si requires further depletion by  $\sim 10$  we expect the Fe requires further depletion by  $\sim 10/2.5 = 4$ . Indeed, the observed [Fe II] line intensity is well below the predicted value based on the model abundance of  $\text{Fe}/\text{H} = 1.7 \times 10^{-7}$ , and requires a gas phase abundance of  $\text{Fe}/\text{H} \sim 4 \times 10^{-8}$ , or  $\sim 1/800$  times the solar value. The depletion is  $\sim 4$ – $6$  times higher than that observed in diffuse clouds (Savage & Sembach 1996) and  $\gtrsim 50$  times higher than that estimated in several PDRs (Okada et al. 2008). Our anomalously high Fe depletion could be a reflection of the higher value of on-SR gas density relative to densities probed in previous studies.

#### 4. GAS HEATING PROCESSES

As was mentioned in the Introduction, previous studies have indicated the presence of low- $J$   $T_{\text{ex}}$  values that seem to be rather high and thus pose a challenge to models of gas heating in PDR environments. Timmermann et al. (1996) found  $T_{\text{ex}} \sim 500 \text{ K}$  in S140 and were able to model observed line intensities by employing an initial gas temperature (at the computational edge of the cloud) of  $T_0 = 1000 \text{ K}$ , as well as  $\cos(\theta) = 0.1$ . Fuente et al. (1999) found a range of  $T_{\text{ex}} \approx 300$ – $700 \text{ K}$  in NGC 7023. Toward the southern half of NGC 2023, Fleming et al. (2010) found  $T_{\text{ex}} \approx 500$ – $1400 \text{ K}$  by fitting  $\text{H}_2$  excitation curves with a single (hot) component over an area larger than the one considered here. Finally, Habart et al. (2011) analyzed *Spitzer* data from a few PDRs with low-valued FUV fields and found OPR-independent ( $\Delta J = 2$ )  $T_{\text{ex}}$  values between  $200$ – $750 \text{ K}$  toward the northern half of NGC 2023.

Our data toward NGC 2023 provide de-zigzagged values of  $T_{\text{ex}}$  that range over  $240$ – $700 \text{ K}$  for on-SR readings and essentially overlap all the pure-rotational results for other PDRs mentioned above. Furthermore, our PDR modeling, which consistently solves for the temperature structure of the gas for each PDR depth layer, shows a  $T_{\text{gas}}$  range of  $300$ – $750 \text{ K}$  over the  $\text{H}_2$  line formation region of, e.g.,  $A_V \sim 0.5$ – $2$ . The close correspondence between  $T_{\text{ex}}$  and  $T_{\text{gas}}$  values calculated by the PDR models



confirms that the pure-rotational  $\text{H}_2$  emission lines detected and analyzed here are primarily thermally excited by collisions rather than radiatively excited by FUV photons.

Figure 13 shows the depth variations of prominent gas heating processes for parameter values  $n_{\text{H}} = 2 \times 10^5 \text{ cm}^{-3}$  and  $\chi = 10^4$ . These processes include grain photoelectric heating as well as heating via collisional de-excitation of FUV pumped  $\text{H}_2$ , and via  $\text{H}_2$  dissociation. Clearly, grain photoelectric heating is dominant throughout the PDR layers where  $\text{H}_2$  line emission arises, with other heating processes contributing  $\lesssim 25\%$  of the heating budget. The successful reproduction of  $\text{H}_2$  data toward NGC 2023 implies that FUV interactions with the dust and gas components of this PDR do not require an additional energy input in the form of mechanical heating from, e.g., turbulence or shocks in this source.

### 5. CONCLUDING REMARKS

The rich molecular spectrum of  $\text{H}_2$  provides a rigorous diagnostic tool in the study of PDRs, the FUV-irradiated envelopes of molecular clouds. We showed that very good agreement can be obtained between modeled and observed absolute values of the line intensities of rotationally-excited  $\text{H}_2$  toward the SR in NGC 2023. According to our PDR models, the highest values of  $\text{H}_2$  emission, which emanate from the narrow SR, require densities up to  $\sim 2 \times 10^5 \text{ cm}^{-3}$  and radiation fields up to  $\sim 10^4$  times the local Galactic field. These values are well within the observationally acceptable range and are consistent with other PDR observables. The agreement between data and models is a direct result of improved sampling of the emission owing to the fine spatial resolution of *Spitzer* instruments, as well as of recent improvements in PDR modeling, including a more detailed treatment of  $\text{H}_2$ , and an enhanced  $\text{H}_2$  formation rate for PDRs. Our results do not confirm the finding by Habart et al. (2011) of order-of-magnitude discrepancies between PDR model results and *Spitzer*  $\text{H}_2$  data, which could be explained by their observations of PDRs illuminated by mainly low-FUV fields. In contrast, for NGC 2023 the FUV field is sufficiently high to dominate any non radiative heating that might be present.

The fact that our model gives a good match to  $\text{H}_2$  rotational line intensities, and to their associated run of increasing  $T_{\text{ex}}$  with  $J$ , is a good indication that the model includes an adequate treatment of heating and cooling processes. In particular, the dominant heating process via photoelectrons is sufficient to maintain the correct  $T_{\text{gas}}$  profile and  $\text{H}_2$  emission distribution within the PDR, without additional mechanical sources of heating. Furthermore, an OPR resulting from H collisions and grain accretion provides a value that is  $\neq 3$  and is matched by fitting both observed and modeled  $\text{H}_2$  column densities. Thus our steady state computation pro-

duces the observed ratios among even- and odd- $J$  states, without the need to artificially adjust the OPR.

According to the PDR model, collisional excitation dominates the pure-rotational emission lines studied here. Thus the curvature of rising  $T_{\text{ex}}$  with  $J$  is not the result of FUV pumping but of collisional thermalization of  $\text{H}_2$  levels in tandem with rising gas temperature within shallower layers of the PDR. In effect, the small fraction of radiative energy from HD 37903 that photoelectrically heats the gas is more important in controlling rotational level populations via collisions than FUV fluorescence.

Our IRS maps show that the decrease in  $\text{H}_2$  emission intensity away from the SR is accompanied by reductions in  $n_{\text{H}}$ ,  $\chi$ , and  $f_{\text{eff}}$ , the latter being the ratio of data to face-on, beam-filled, normally-illuminated model intensity. The analysis of the four factors that affect the value of  $f_{\text{eff}}$  indicated that its reduction may be facilitated by a combined reduction in inclination and incidence factors, which are countered by a more modest increase in the value of the beam-filling factor. Despite the difficulty of constraining all factors, the observations were shown to be consistent with a previously (Field et al. 1994) suggested 3-D structure of the region around the SR, namely a quasi-pyramidal molecular cloud towering above the FUV-carved cavity toward HD 37903.

The successful interplay between PDR observations and theory supports the description of NGC 2023 as a *par excellence* example of a photodissociation region. This is especially significant because the results presented here require the shorter distance scale for HD 37903. Indeed, a very recent re-examination of the SIMBAD database on 2011 May 20 at 12:20 EDT revealed a newly published revision of the *HIPPARCOS* parallaxes based on van Leeuwen (2007). One of these parallaxes provides a new distance to HD 37903 of  $300^{+110}_{-60}$  pc, predicting an on-SR  $\chi$  of  $(1.03^{+0.58}_{-0.48}) \times 10^4$ , which is in extremely good agreement with our PDR modeling results.

YS thanks Dr. Frédéric Galliano, whose table, chair, and a very useful suite of start-up IDL routines were inherited by YS upon arrival at UMCP. This work was supported in part by NASA through an award issued by JPL/Caltech and is based on observations made with the *Spitzer* Space Telescope, which is operated by the Jet Propulsion Laboratory, California Institute of Technology under NASA contract 1407. YS and MGW were supported in part by a NASA Long Term Space Astrophysics Grant NNG05G64G. MJK and MC were supported by NSF grant PHY-0552964 for the REU program in Physics and Astronomy at San Jose State University. This research has made use of the SIMBAD database, operated at CDS, Strasbourg, France.

Facilities: *Spitzer* (IRS, IRAC), ESO: VISTA, HST (ACS)

### REFERENCES

- Allers, K. N., Jaffe, D. T., Lacy, J. H., Draine, B. T., & Richter, M. J. 2005, *ApJ*, 630, 368
- Anthony-Twarog, B. J. 1982, *AJ*, 87, 1213
- Beirão, P., Brandl, B. R., Appleton, P. N., et al. 2008, *ApJ*, 676, 304
- Brandl, B. R., Devost, D., Higdon, S. J. U., et al. 2004, *ApJS*, 154, 188
- Burton, M. 1993, *Pub. Astr. Soc. Aus.*, 10, 322
- Burton, M. G., Hollenbach, D. J., & Tielens, A. G. G. M. 1990, *ApJ*, 365, 620
- Burton, M. G., Hollenbach, D. J., & Tielens, A. G. G. 1992, *ApJ*, 399, 563
- Burton, M. G., Howe, J. E., Geballe, T. R., & Brand, P. W. J. L. 1998, *Pub. Astr. Soc. Aus.*, 15, 194

- Caballero, J. A. 2008, MNRAS, 383, 750
- Conti, P. S., Crowther, P. A., & Leitherer, C. 2008, in “From Luminous Hot Stars to Starburst Galaxies”, Cambridge University Press
- Dale, D. A., Smith, J. D. T., Schlawin, E. A., et al. 2009, ApJ, 693, 1821
- Dedes, C., Röllig, M., Mookerjee, B., et al. 2010, A&A, 521, L24
- DePoy, D. L., Lada, E. A., Gatley, I., & Probst, R. 1990, ApJ, 356, L55
- Draine, B. T. 1978, ApJS, 36, 595
- Draine, B. T., & Bertoldi, F. 1996, ApJ, 468, 269
- Draine, B. T., & Bertoldi, F. 2000, in Molecular Hydrogen in Space, eds. Combes, F., & Pineau des Forêts, G., Cambridge University Press, Cambridge, p. 131
- Falgarone, E., Verstraete, L., Pineau des Forêts, G., Hily-Blant, P. 2005 A&A, 433, 997
- Field, D., Gerin, M., Leach, S., Lemaire, J. L., Pineau des Forêts, G., Rostas, F., Rouan, D., & Simons, D. 1994, A&A, 286, 909
- Field, D., Lemaire, J. L., Pineau des Forêts, G., Gerin, M., Leach, S., Rostas, F., & Rouan, D. 1998, A&A, 333, 280
- Fleming, B., France, K., Lupu, R. E., & McCandliss, S. R. 2010, ApJ, 725, 159
- Fuente, A., Martín-Pintado, J., Rodríguez-Fernández, N. J., Rodríguez-Franco, A., de Vicente, P., & Kunze, D. 1999, ApJ, 518, L45
- Galliano, F., Madden, S. C., Tielens, A. G. G. M., Peeters, E., & Jones, A. P. 2008, ApJ, 679, 310
- Gatley, I. & Kaifu, N. 1987, IAU Symp., 120, 153
- Goldsmith, P. F., Velusamy, T., Li, D., & Langer, W. D. 2010, ApJ, 715, 1370
- Habart, E., Boulanger, F., Verstraete, L., Walmsley, C. M., & Pineau des Forêts, G. 2004, A&A, 414, 531
- Habart, E., Abergel, A., Boulanger, F., Joblin, C., Verstraete, L., Compiègne, M., Pineau des Forêts, G., & Le Bourlot, J. 2011, A&A, 527, 122
- Heyer, M., Krawczyk, C., Duval, J., & Jackson, J. M. 2009, ApJ, 699, 1092
- Hasegawa, T., Gatley, I., Garden, R. P., Brand, W. J. L., Ohishi, M., Hayashi, M., & Kaifu, N. 1987, ApJ, 318, L77
- Herbst, T. M., Beckwith, S. V., Glindemann, A., Tacconi-Garman, L. E., Kroker, H., & Krabbe, A. 1996, AJ, 111, 2403
- Hollenbach, D., Kaufman, M. J., Bergin, E. A., & Melnick, G. J. 2009, ApJ, 690, 1497
- Houck, J. R., Roellig, T. L., van Cleve, J., et al. 2004, ApJS, 154, 18
- Jaffe, D. T., Genzel, R., Harris, A. I., Howe, J. E., Stacey, G. J., & Stutzki, J. 1990, ApJ, 353, 193
- Kaufman, M. J., Wolfire, M. G., Hollenbach, D. J., & Luhman, M. L. 1999, ApJ, 527, 795
- Kaufman, M. J., Wolfire, M. G., & Hollenbach, D. J. 2006, ApJ, 644, 283
- Le Bourlot, J. 2000, A&A, 360, 656
- Le Petit, F., Nehmé, C., Le Bourlot, J., & Roueff, E. 2006, ApJS, 164, 506
- Maret, S., Bergin, E. A., Neufeld, D. A., et al. 2009, ApJ, 698, 1244
- Martini, P., Sellgren, K., & DePoy, D. L. 1999, ApJ, 526, 772
- Mathis, J. S. 1990, ARA&A, 28, 37
- Menten, K. M., Reid, M. J., Forbrich, J., Brunthaler, A. 2007, A&A, 474, 515
- Mookerjee, B., Sandell, G., Jarrett, T. H., & McMullin, J. P. 2009, A&A, 507, 1485
- Neufeld, D. A., Melnick, G. J., Sonnentrucker, P., et al. 2006, ApJ, 649, 816
- Neufeld, D. A., Nisini, B., Giannini, T., et al. 2009, ApJ, 706, 170
- Okada, Y., Onaka, T., Miyata, T., Okamoto, Y. K., Sakon, I., Shibai, H., & Takahashi, H. 2008, ApJ, 682, 416
- Parravano, A., Hollenbach, D. J., & McKee, C. F. 2003, ApJ, 584, 797
- Perryman, M. A. C., Lindegren, L., Kovalevsky, J., et al. 1997, A&A, 323, L49
- Quanz, S. P., Henning, Th., Bouwman, J., Linz, H., & Lahuis, F. 2007, ApJ, 658, 487
- Sandstrom, K. M., Peek, J. E. G., Bower, G. C., Bolatto, A. D., Plambeck, R. L. 2007, ApJ, 667, 1161
- Savage, B. D. & Sembach, K. R. 1996, ARA&A, 34, 279
- Sellgren, K. 1983, AJ, 88, 985
- Sheffer, Y., Prochaska, J. X., Draine, B. T., Perley, D. A., & Bloom, J. S. 2009, ApJ, 701, L63
- Smith, J. D. T., Armus, L., Dale, D. A., et al. 2007, PASP, 119, 1133
- Solomon, P. M., Rivolo, A. R., Barrett, J., & Yahil, A. 1987, ApJ, 319, 730
- Steiman-Cameron, T. Y., Haas, M. R., Tielens, A. G. G. M., & Burton, M. G. 1997, ApJ, 478, 261
- Sternberg, A., & Dalgarno, A. 1989, ApJ, 338, 197
- Sternberg, A., & Dalgarno, A. 1995, ApJS, 99, 565
- Sternberg, A., & Neufeld, D. A. 1999, ApJ, 516, 371
- Tielens, A. G. G. M., & Hollenbach, D. 1985, ApJ, 291, 722
- Timmermann, R., Bertoldi, F., Wright, C. M., Drapatz, S., Draine, B. T., Haser, L., & Sternberg, A. 1999, A&A, 315, L281
- van Leeuwen, F. 2007, A&A, 474, 653
- Weingartner, J. C., & Draine, B. T. 1999, in The Universe as seen by ISO, Eds. P. Cox and M. F. Kessler, ESA Special Publications Series (SP-427), p. 783
- Wolfire, M. G., Hollenbach, D., & McKee, C. F. 2010, ApJ, 716, 1191
- Wolfire, M. G., McKee, C. F., Hollenbach, D., & Tielens, A. G. G. M. 2003, ApJ, 587, 278
- Wyrowski, F., Walmsley, C. M., Natta, A., Tielens, A. G. G. M. 1997, A&A, 324, 1135
- Wyrowski, F., Walmsley, C. M., Goss, W. M., Tielens, A. G. G. M. 2000, ApJ, 543, 245

TABLE 1  
LOG OF *Spitzer* OBSERVATIONS OF NGC 2023

Module	Pixel ( $''$ )	Slit ( $'' \times ''$ )	AOR	Object	Date	$\alpha$ (J2000)	$\delta$ (J2000)	Exposures ( $\# \times s$ )
SH	2.26	$4.7 \times 11.3$	14033920	NGC 2023	2006/03/19	05:41:37.63	−02:16:42.6	$144 \times 30$
LH	4.46	$11.1 \times 22.3$	14034176	NGC 2023	2006/03/19	05:41:37.63	−02:16:42.6	$30 \times 60$
SL	1.85	$3.7 \times 57$	17977856	NGC 2023	2007/10/08	05:41:37.63	−02:16:42.6	$54 \times 28$
SL	1.85	$3.7 \times 57$	17978112	Sky bkgd	2007/10/08	05:40:26.21	−02:54:40.3	$4 \times 28$

TABLE 2  
GAUSSFIT PARAMETERS<sup>a</sup> AND THEIR UNCERTAINTIES<sup>b</sup>

Line	$\lambda_{\text{rest}}$ ( $\mu\text{m}$ )	$A_0^c$ ( $10^{-5}$ )	$A_1$ ( $\mu\text{m}$ )	$A_1 - \lambda_{\text{rest}}$ ( $\mu\text{m}$ )	$A_2$ ( $\mu\text{m}$ )	$R^d$	$\Sigma A_0^c$ ( $10^{-5}$ )
Map Median (off-SR)							
S(0)	28.2188	1.35(8)	28.225(1)	+0.006	0.015(1)	804(65)	2.3(2)
S(1)	17.0348	5.84(9)	17.0378(2)	+0.003	0.0106(2)	680(12)	11.6(3)
S(2)	12.2786	6.9(1)	12.2801(1)	+0.001	0.0071(1)	736(14)	13.5(4)
S(3)	9.6649	9.2(2)	9.663(1)	−0.002	0.053(2)	78(2)	19.6(8)
S(5)	6.9095	4.1(5)	6.905(3)	−0.005	0.030(4)	98(12)	9(2)
R.u. <sup>e</sup>		2—12%	0.001—0.04%		2—12%	2—12%	3—18%
Single Pixel [7:8] (on-SR)							
S(0)	28.2188	1.7(1)	28.2231(7)	+0.004	0.014(1)	844(64)	2.8(3)
S(1)	17.0348	14.8(2)	17.0380(2)	+0.003	0.0105(2)	688(13)	29.4(7)
S(2)	12.2786	18.8(2)	12.2798(1)	+0.0008	0.0068(1)	772(13)	33.8(7)
S(3)	9.6649	40.8(4)	9.6689(5)	+0.004	0.0511(6)	80.3(9)	84(1)
S(5)	6.9095	22(1)	6.912(2)	+0.002	0.031(2)	95(6)	54(4)
R.u. <sup>e</sup>		1—6%	0.001—0.02%		1—8%	1—8%	1—9%

<sup>a</sup> Each line is fitted with  $I(\lambda) = A_0 \exp(-0.5[\lambda - A_1]^2/A_2^2) + A_3 + A_4\lambda$ ; the continuum (last two terms) is subtracted from the fit.

<sup>b</sup> Uncertainties for the last digits are in parentheses.

<sup>c</sup> Units for  $A_0$  are  $\text{erg s}^{-1} \text{cm}^{-2} \text{sr}^{-1}$ ;  $\Sigma A_0$  = integrated line intensity, with conservative uncertainty taken from  $A_0$  &  $A_2$  in quadratures.

<sup>d</sup>  $R \equiv \lambda_{\text{rest}}/(2.355A_2)$  is the spectral resolution.

<sup>e</sup> R.u.  $\equiv$  Relative uncertainty.

TABLE 3  
NORMAL MODEL MAPPING OF NGC 2023-SOUTH

Map region (# of pixels)	$n_{\text{H}}^a$ (dex)	$\chi$	RMSD (dex)	$f_{\text{eff}}^b$	$\chi/n_{\text{H}}$
Model: $\log n_{\text{H}} = 5.0$ ; $\log \chi = 3.7$					
Global (170)	5.0	5000.	0.104	0.50	0.05
On-SR (15)	5.0	5000.	0.144	1.07	0.05
Off-SR-S (9)	5.0	5000.	0.104	0.60	0.05
Off-SR-N (12)	5.0	5000.	0.134	0.37	0.05
Grid: $\log n_{\text{H}} = 4.7\text{—}5.3$ ; $\log \chi = 3.6\text{—}4.2$					
Global (170)	5.0	8000.	0.062	0.49	0.08
On-SR (15)	5.2	10000.	0.062	0.74	0.06
Off-SR-S (9)	5.1	6000.	0.075	0.48	0.05
Off-SR-N (12)	4.9	6000.	0.064	0.49	0.08

NOTE. — Values are sample medians.

<sup>a</sup> Number density units are  $\text{cm}^{-3}$ .

<sup>b</sup> Ratio of data/model.

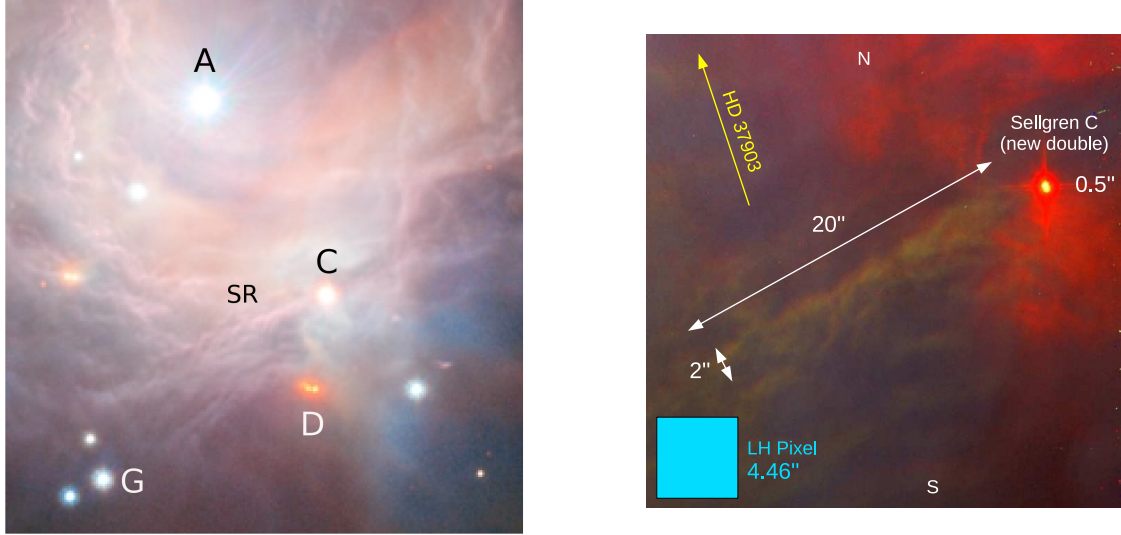


FIG. 1.— Left panel shows a near-infrared view of the southern half of NGC 2023 as combined from J (“blue”), H (“green”), and K (“red”) exposures. This highly magnified region of size  $\approx 3' \times 3'$  shows HD 37903 (Sellgren A) as the brightest star toward the top, and a pink-colored Southern Ridge (SR) just below the center of the image. Additional stars are identified by their Sellgren letters. Credit: ESO/J. Emerson/VISTA/Cambridge Astronomical Survey Unit (ESO release 0949). Right panel shows a magnified region of  $\approx 30'' \times 30''$  from an *HST*-ACS image, providing the highest angular resolution view of the SR to date. A blue square shows the size of an LH pixel from *Spitzer*-IRS. All figure labels were inserted manually and should not be presumed to have a level of precision better than 10%. Credit: [http://en.wikipedia.org/wiki/NGC\\_2023](http://en.wikipedia.org/wiki/NGC_2023), based on ACS data set j8mw01.

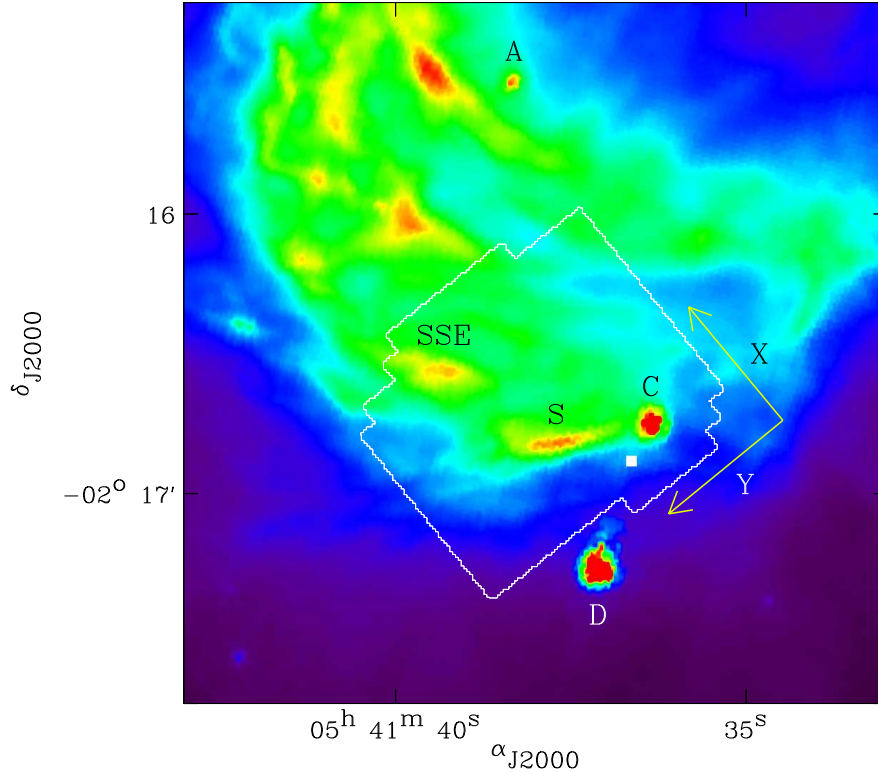


FIG. 2.— IRS all-module common field (irregular outline) overlaying the IRAC channel 4 image of NGC 2023, which is dominated by PAH emission at  $8\ \mu\text{m}$ . All maps to follow shall employ the instrumental orientation (vectors X, Y). As in left panel of Figure 1, Sellgren A is the IR-faint HD 37903, whereas Sellgren C and D are two IR-bright young stellar objects. S is the SR, a narrow  $\text{H}_2$  emission filament, whereas SSE is the South-Southeastern Ridge, a wider emission clump.

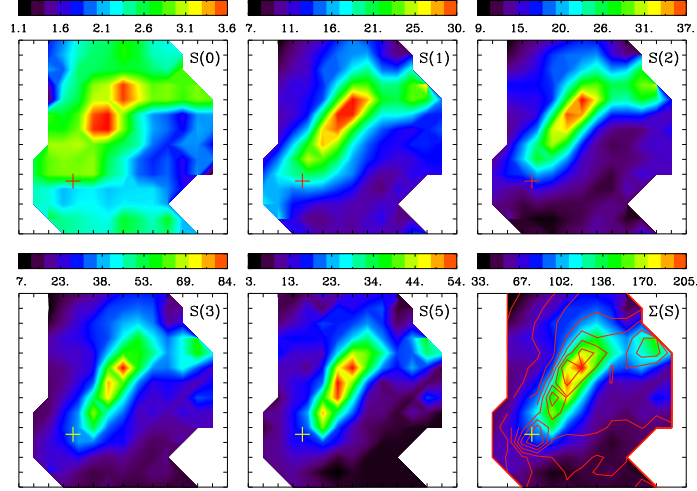


FIG. 3.— Intensity maps of  $\text{H}_2$  line emission (uncorrected for extinction) toward the SR of NGC 2023. The color bars show the intensity scale in units of  $10^{-5} \text{ erg s}^{-1} \text{ cm}^{-2} \text{ sr}^{-1}$ . Each box spans  $14 \times 13$  pixels, or  $\approx 1' \times 1'$ . First five panels from top left show detected transitions from  $J = 2, 3, 4, 5$  and  $7$  in the observed LH frame. Last panel employs the total intensity of all five emission lines as a background for contours of continuum intensity from the  $8 \mu\text{m}$  IRAC image shown in Figure 2. The ‘+’ indicates the position of Sellgren C.

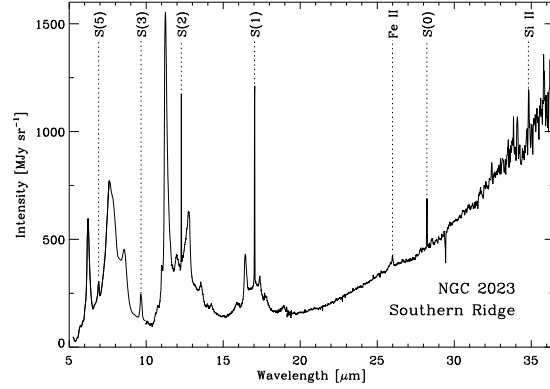


FIG. 4.— Full spectral coverage from the four IRS modules SL2, SL1, SH, and LH toward NGC 2023, as obtained by averaging 15 pixels that sample SR emission.  $\text{H}_2$  and atomic emission lines are identified, and their rest wavelengths are indicated by dotted lines. Strong PAH features and dust continuum are evident.

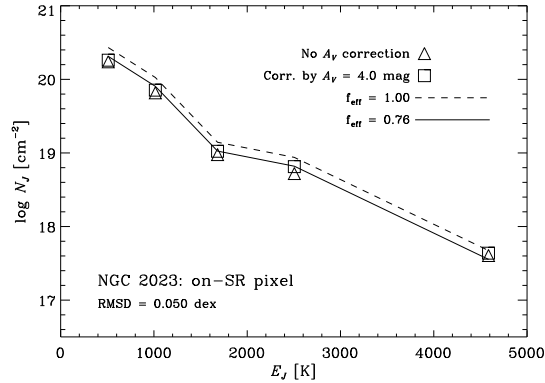


FIG. 5.— Observed  $N_J$  values (symbols) for the single on-SR pixel LH[7:8] compared with model results (lines). Boxes show  $\Delta N_J = \pm 20\%$  corrected for  $A_V = 4.0 \text{ mag}$  and triangles show the data prior to extinction correction. The dashed line shows the unshifted  $\log n_{\text{H}} = 5.3$  and  $\chi = 10^4$  model. The solid line shows the same model shifted by  $-0.12 \text{ dex}$ , or  $f_{\text{eff}} = 0.76$  (see text), following RMSD minimization.

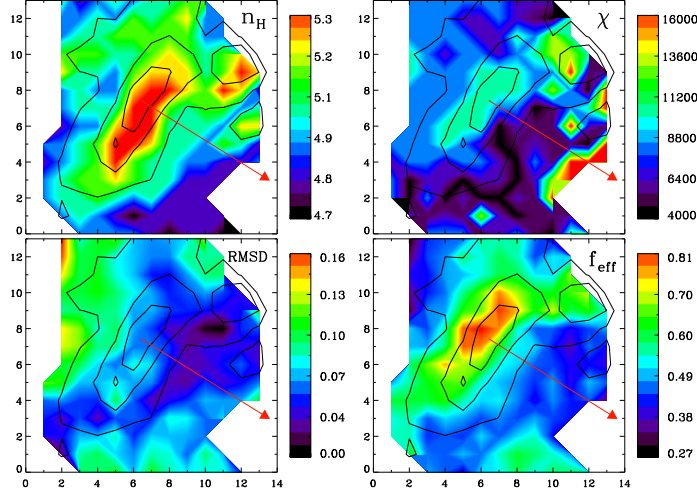


FIG. 6.— Mapping of NGC 2023 with a grid of normal models. Upper left: logarithmic map of gas density variations. Upper right: linear map of FUV flux variations. Lower left: RMSD values are  $\leq 0.16$  dex over the map. Lower right: ratio of data to model required to minimize the RMSD. Each box spans  $14 \times 13$  pixels, or  $\approx 1' \times 1'$ . Contours show the 30, 50 and 75% levels of the total intensity of all five  $\text{H}_2$  emission lines (from last panel of Figure 3). Red arrows extend exactly one half the distance toward HD 37903.

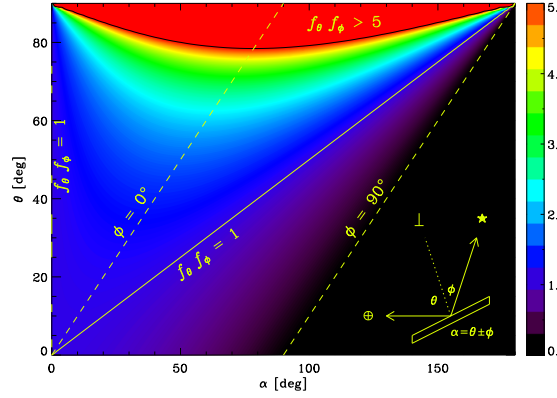


FIG. 7.— Product  $f_\theta f_\phi \equiv \cos(\phi)/\cos(\theta)$  is contoured as a function of  $\alpha$  and  $\theta$ . As depicted in the lower right corner,  $\alpha$  is the angle at the source between HD 37903 ( $\star$ ) and our line of sight ( $\oplus$ ),  $\theta$  is the surface inclination of the source, whose normal is indicated by ' $\perp$ ', and  $\phi$  is the angle of FUV incidence. All values above upper limit of color bar (black contour of  $f_\theta f_\phi = 5$ ) are mono-colored red.

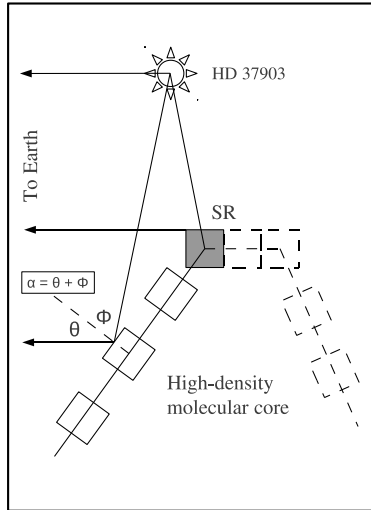


FIG. 8.— Cross-sectional cartoon of the suggested 3-D structure of NGC 2023 in the vicinity of the SR. The SR sits on top of a quasi-pyramidal high-density molecular core, the surface of which is made up of parallel cloud ridges that are subject to reduced levels of FUV irradiation. This core harbors the heavily obscured formation site of Sellgren D, see Figures 1 and 2.

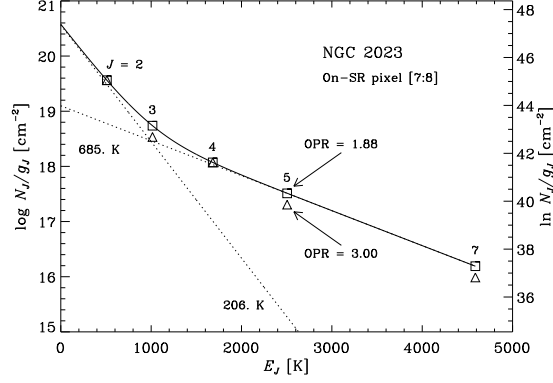


FIG. 9.— Excitation diagram for the on-SR pixel LH[7:8]. Data boxes are  $\pm 20\%$  in vertical extent, owing to IRS uncertainty. The data were de-zigzagged by shifting the odd- $J$  values for OPR = 3 (triangles) toward the even- $J$  levels, while minimizing the RMSD between the smooth excitation curve and the data. This pixel is found to have OPR  $\approx 1.9$ , with “cold” and “hot”  $T_{\text{ex}}$  of 206 and 685 K, respectively (dashed lines), see also Figure 12.

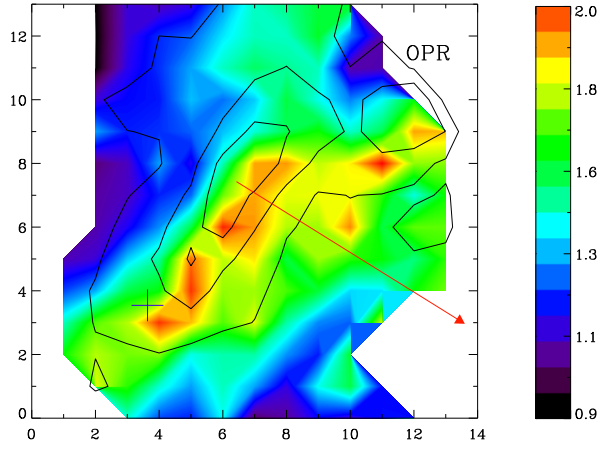


FIG. 10.— Spatial variation of the OPR over the LH field toward NGC 2023. Box size is  $14 \times 13$  pixels, or  $\approx 1' \times 1'$ . Total  $\text{H}_2$  on-SR intensity is indicated by contour levels of 30, 50 and 75%, with the red arrow extending half the distance toward HD 37903 and the location of star C marked by ‘+’.

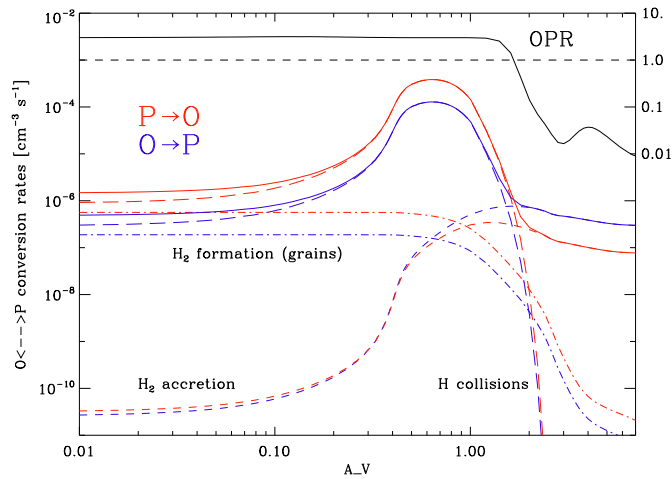


FIG. 11.— Three OPR-controlling processes and their sum are plotted as a function of depth into the PDR. Each process is found to dominate  $\text{o-H}_2 \rightleftharpoons \text{p-H}_2$  conversions over a certain range of  $A_V$ . At  $A_V \lesssim 1.5$ ,  $\text{p-H}_2 \rightarrow \text{o-H}_2$  domination maintains an OPR of  $\approx 3$  (see scale on the right), but deeper into the PDR,  $\text{o-H}_2 \rightarrow \text{p-H}_2$  dominates owing to  $\text{H}_2$  accretion onto cold dust and is responsible for a rapid decline of the OPR. A horizontal dashed line shows the level of OPR = 1.

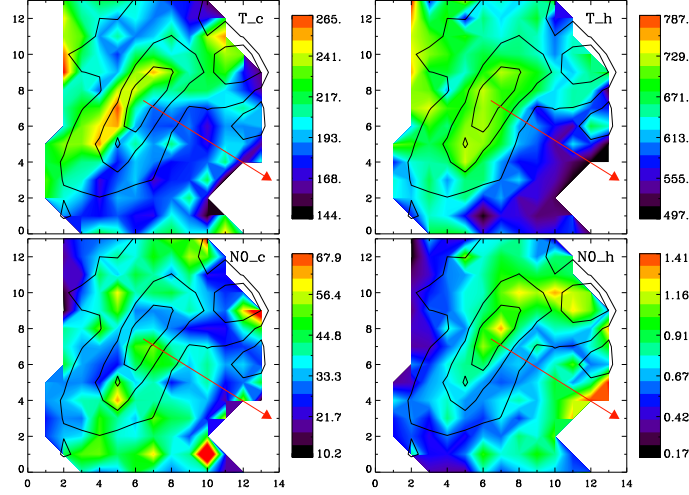


FIG. 12.— Upper panels: mapping of  $T_{\text{ex}}^{\text{cold}}$  (left) and  $T_{\text{ex}}^{\text{hot}}$  (right) toward the SR, both in K. Lower panels: mapping of  $N_0^{\text{cold}}$  (left) and  $N_0^{\text{hot}}$  (right), both in  $10^{19} \text{ cm}^{-2}$ . These  $14 \times 13$  pixel ( $\approx 1' \times 1'$ ) maps are by-products of the OPR de-zigzagging procedure as demonstrated in Figure 9. Red arrows extend half the distance toward HD 37903.

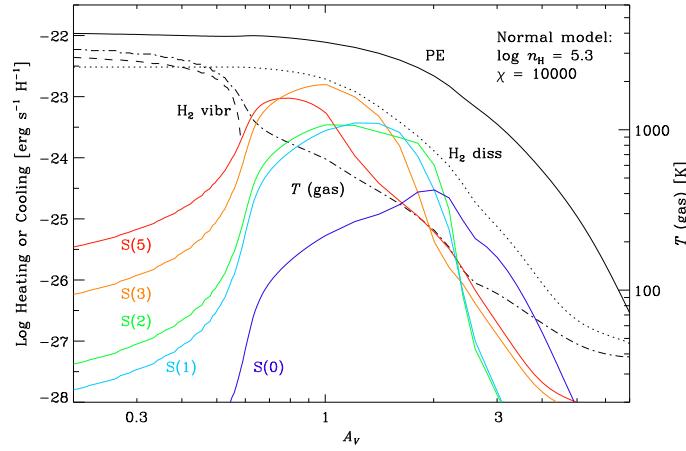


FIG. 13.— Modeled heating processes in the gas for a normal model with  $n_{\text{H}} = 2 \times 10^5 \text{ cm}^{-3}$  and  $\chi = 10^4$ . Heating is controlled by photoelectric emission from grains (“PE”, solid curve) throughout the  $\text{H}_2$  line formation region indicated by colored emissivity (cooling) curves. Lesser heating contributions are from  $\text{H}_2$  dissociation (dotted curve) and from  $\text{H}_2$  ro-vibrational de-excitation (dashed curve plotted is net heating minus cooling). The dot-dashed curve shows the gas temperature profile, with scale on the right.